

## Supporting Information

### Highly flexible and compact magnetoresistive analytic devices

Gungun Lin<sup>a,b\*</sup>, Denys Makarov<sup>a\*</sup>, Michael Melzer<sup>a</sup>, Wenping Si<sup>a,b</sup>, Chenglin Yan<sup>a,c</sup> and Oliver G. Schmidt<sup>a,b</sup>

<sup>a</sup> Institute for Integrative Nanosciences, IFW Dresden, Helmholtzstr. 20, 01069 Dresden, Germany;

<sup>b</sup> Material Systems for Nanoelectronics, Chemnitz University of Technology, Reichenhainerstr. 70, 09107 Chemnitz, Germany;

<sup>c</sup> School of Energy, Soochow University, 215006 Suzhou, Jiangsu, People's Republic of China;

\* Corresponding authors: g.lin@ifw-dresden.de; d.makarov@ifw-dresden.de

**Magnetolectrical characterizations for GMR multilayers on different substrates:** We prepared [Py(1.9 nm)/Cu(0.9 nm)]<sub>30</sub> and [Py(1.5 nm)/Cu(2.3 nm)]<sub>30</sub> which are exchange coupled at the 1<sup>st</sup> and 2<sup>nd</sup> interlayer antiferromagnetic maximum, respectively. We observed (**Fig. S1**) that for samples deposited directly on PET foils there is a reduction of GMR ratio, compared with the one deposited directly on silicon substrate. However, by introducing SU-8 polymer as a buffer layer, GMR ratio for both series of samples (1<sup>st</sup> and 2<sup>nd</sup> maximum) is retained.

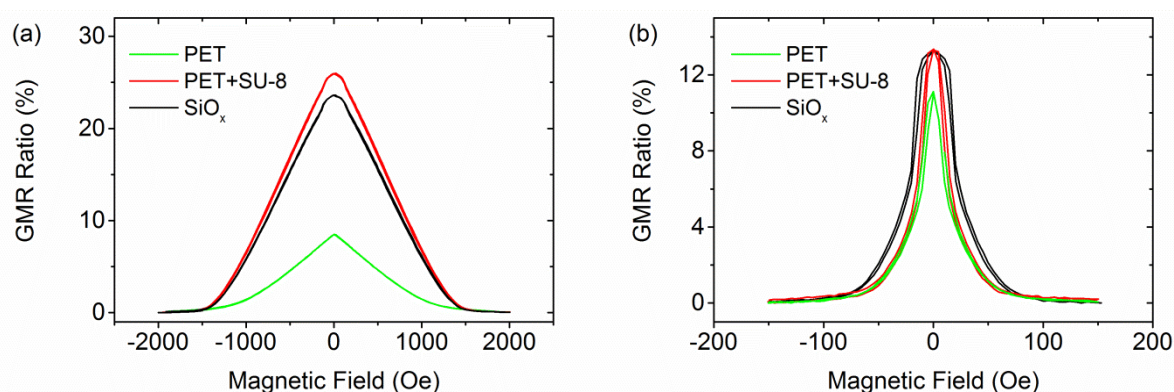


**Fig. S1** | GMR curves for [Py(1.9 nm)/Cu(0.9 nm)]<sub>30</sub> (a) and [Py(1.5 nm)/Cu(2.3 nm)]<sub>30</sub> (b) prepared on PET foil, SU-8-buffered PET foil and silicon substrate.

**AFM measurements of substrates:** The enhancement of GMR ratio was studied by AFM measurements on different substrates (**Fig. S2**). For a bare PET foil, a root mean square roughness of 15 nm over an area of  $10 \times 10 \mu\text{m}^2$  is observed, which is characterized with lots of big islands on the surface. For a silicon substrate (covered with 600 nm silicon oxide), the surface roughness is about 0.4 nm. For the SU-8-buffered PET foil, the roughness (0.3 nm) is greatly reduced, which is slightly smaller than silicon substrate. This explains the distinct GMR ratio of samples prepared on different substrates. GMR effect is an interfacial mediated phenomenon and is dependent on the strength of the interlayer exchange coupling which can be enhanced by reducing surface roughness<sup>[s1]</sup>.

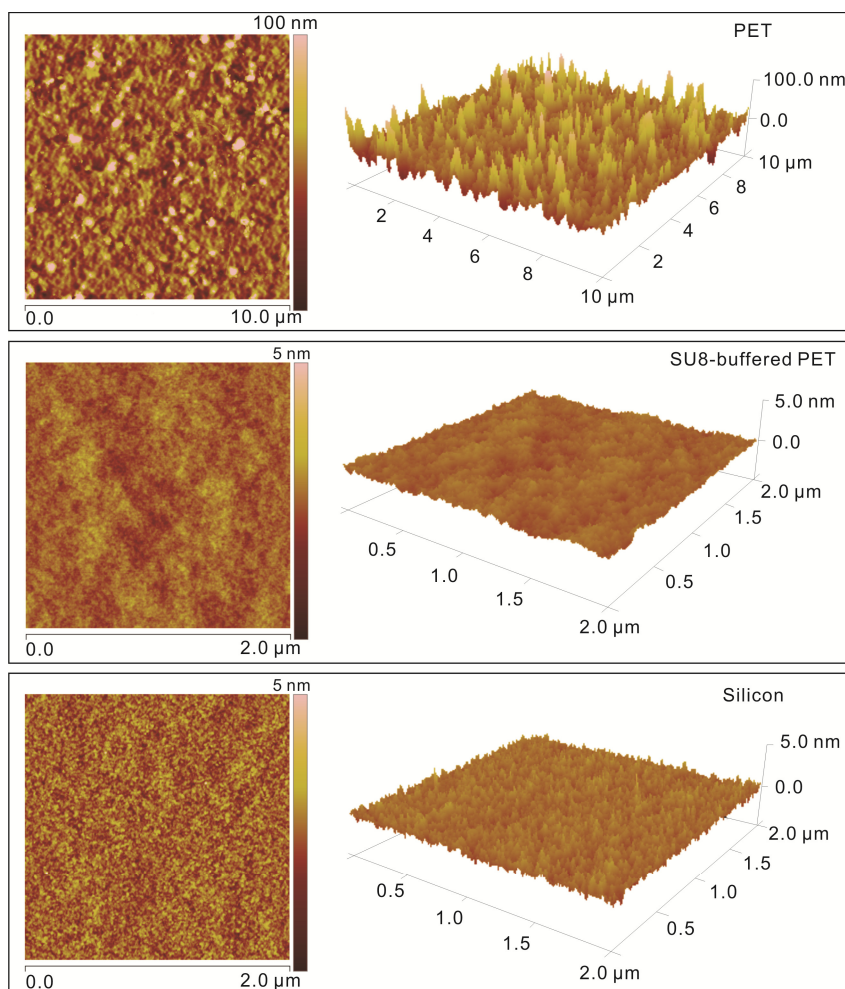


**Fig. S2** | AFM measurements of PET foil, SU-8-buffered PET foil, and silicon substrate.

For the PET foil, the measured area is  $10 \times 10 \mu\text{m}^2$ , while for the SU8-buffered PET and the silicon substrate, the measured area is  $2 \times 2 \mu\text{m}^2$ .

**Real time measurement setup:** A schematic sketch of the real time measurement setup is illustrated in **Fig. S3**, which is based on a Wheatstone bridge circuitry to achieve high measurement sensitivity. Three trimmers  $R_1$ ,  $R_2$  and  $R_3$  were used to minimize the background level. The sensor was powered by a lock-in amplifier, the differential voltage signal  $\Delta V$  of which was fed in to the lock-in to amplify the signal and reduce the noise. The analogue output from the lock-in was picked up by an analogue/digital converter (NI-USB 6800, National Instrument). The sampling rate of the AD converter is 5 kHz. The measurement range of the lock-in was 500  $\mu\text{V}$ . For the measurement, an external permanent magnet is placed below the sensor. As the sensor is sensitive to the in-plane magnetic field, the in-plane component of the stray fields from the magnet is used to bias the sensor to the most sensitive region. The position of the magnet was carefully adjusted via monitoring the sensor output and fixed during the whole measurement of droplets.

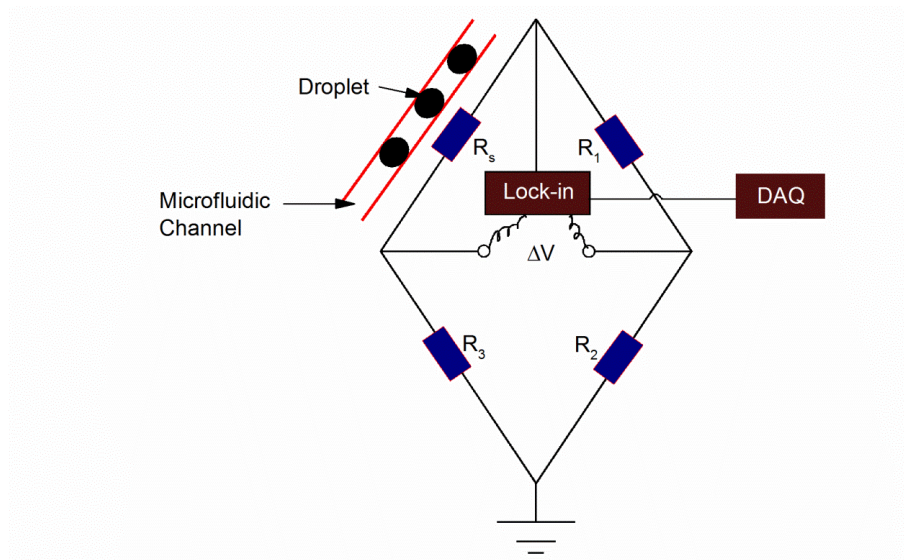


**Fig. S3** | Schematic sketch of the real time measurement setup. The GMR sensor ( $R_s$ ) is in connection with three additional resistors ( $R_1$ ,  $R_2$ , and  $R_3$ ) to form a Wheatstone bridge. When droplets are passing across an integrated GMR sensor in the microfluidic channel, the differential voltage ( $\Delta V$ ) of the bridge was fed into the lock-in and

amplified. The output of the lock-in is picked up by a data acquisition box (DAQ, NI-USB 6008).

**Droplet generator:** A T-junction geometry shown in **Fig. S4** was fabricated to produce magnetic emulsion droplets on chip. Magnetic nanoparticles diluted with DI water served as a disperse phase. Hydrocarbon oil was used as a continuous phase. The injection directions of both phases are pointed out according to the arrows. The magnetic nanoparticles and oil were pumped into the device by a controlled syringe pump (NEMESYS, Cetoni GmbH) with a total flowing rate of 15 nl/s. The flow rate of oil and magnetic nanoparticles were adjusted to produce droplets of various dimensions for measurements.

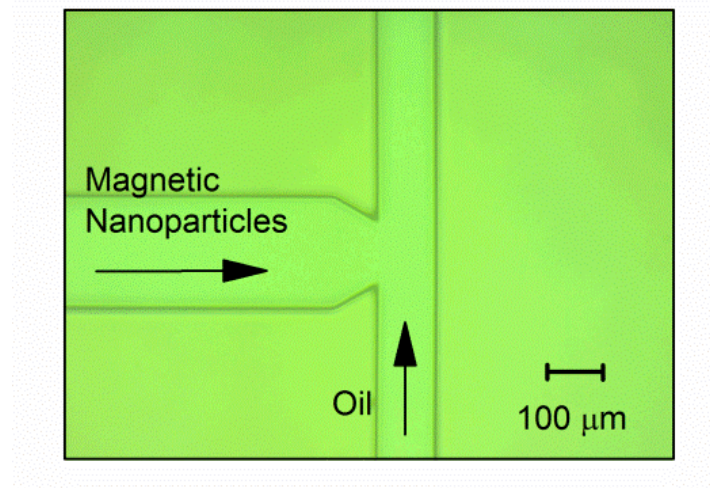


**Fig. S4** | Optical microphotograph of a T-junction design fabricated on the chip for the formation of magnetic emulsions.

**Determination of intrinsic GMR ratio:** To determine the intrinsic GMR ratio of GMR sensors which are micro-patterned into rectangular stripes with width of 6  $\mu\text{m}$  and different length of 20, 40, 60 and 100  $\mu\text{m}$  (**Fig. S5b**). The intrinsic GMR ratio is defined as:  $\text{GMR} = (R(H_{\text{ext}}) - R(H_{\text{sat}}))/R(H_{\text{sat}})$ .<sup>[s2]</sup>

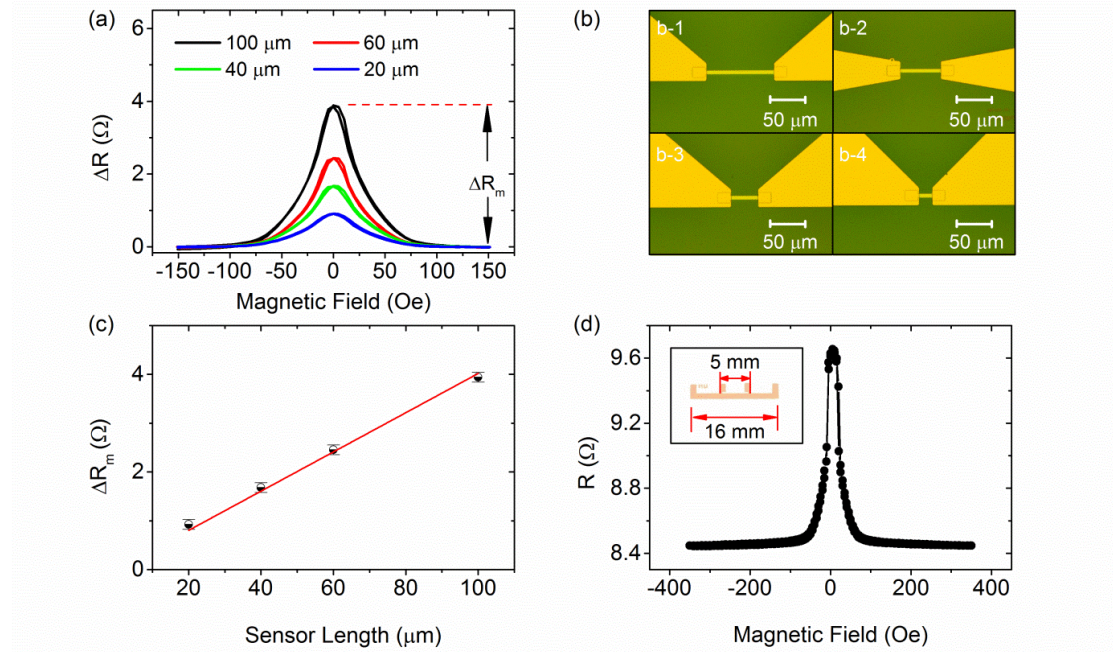


**Fig. S5** | (a) Magneto-electrical characterizations of different GMR sensor stripes patterned on a polymer-buffered PET foil. (b) Microscopic photographs of the GMR sensor stripes with different length: 100  $\mu\text{m}$  (b-1), 60  $\mu\text{m}$  (b-2), 40  $\mu\text{m}$  (b-3), and 20  $\mu\text{m}$  (b-4). (c) Plot of the maximum change of the sensor resistance with the length of the GMR sensor stripe. (d) Magneto-electrical characterization of a GMR sensor patterned into standard four-probe geometry (inset) with a dimension of 1 x 16  $\text{mm}^2$ .

As the GMR sensor stripes were patterned with two-point geometry, the intrinsic GMR ratio was derived by excluding contact resistance. **Fig. S5a** shows the change of the sensor resistance with an external magnetic field for different sensor stripes, which is given by:<sup>[s3]</sup>  $\Delta R = (R_q \times \text{GMR}/w)l_s$ , where  $\Delta R$  is the change of the sensor resistance with the magnetic field,  $l_s$  is the length of the sensor,  $w$  is the width of the sensor, and  $R_q$  is the square sensor resistance which can be derived from a patterned GMR sensor of 1 x

16 mm<sup>2</sup> with 4-point geometry (**Fig. S5d**). For GMR sensor stripes of the same layer stack ( $R_q = 1.69 \Omega$ ) and width ( $w = 6 \mu\text{m}$ ),  $\Delta R$  scales with  $l_s$  if the GMR ratio of these GMR sensor stripes is the same. **Fig. S5c** shows that  $\Delta R$  scales with  $l_s$  with slope of  $0.04 \Omega \cdot \mu\text{m}^{-1}$  indicating that these patterned GMR stripes as shown in **Fig. S5b** share an identical intrinsic GMR ratio at the level of 14%, which can be derived from:  $\text{GMR} = kw/R_q$ , with  $k$  being the slope of the linear plot of  $\Delta R$  against  $l_s$ .

**Bending Experiments:** The bending experiment was carried out by using the experimental setup shown in **Fig. S6a, b**. Details of the working principle are described in the experimental section. We bent the device continuously until two ends of the device were almost closed (**Fig. S6d**). Also cyclic bending of the device to constant radius of 8 mm was performed (**Fig. S6e**). The sample resistance was recorded at zero magnetic field and at an external magnetic field of 300 Oe, respectively. Both indicate that the whole device was well electrically contacted without showing any degradation in performance.

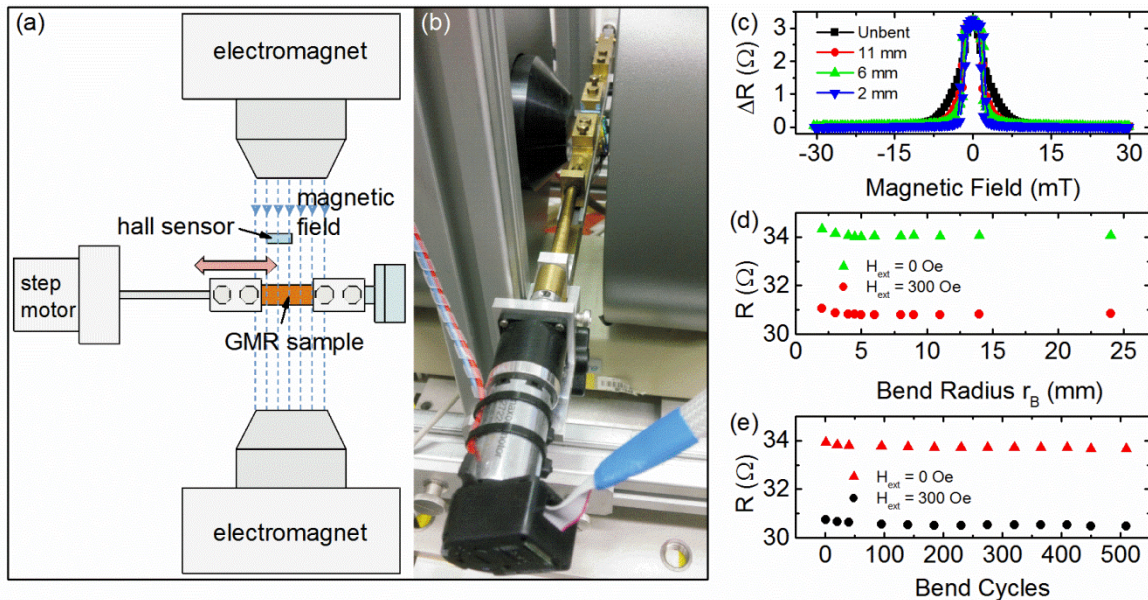


**Fig. S6** | Schematic sketch (a) and photograph (b) of the experimental setup for bending tests and magnetoelectrical characterizations. The change of resistance under cyclic magnetic fields (c) as well as the total resistance of the device (d) at different bended states, and when it is reversibly bent to radius of 8 mm with different bending cycles (d). To demonstrate an effective flexible microfluidic device, the device was connected to external tubes where magnetic nanoparticles and oil can be injected via two separate inlets to form emulsion droplets. Two ends of the device were gradually closed (**Fig. S7**) to minimum bending radius of 2 mm. We observe that emulsion droplets were well produced even at extremely bended state (radius of 2 mm), indicating the robustness of the device against external deformations.

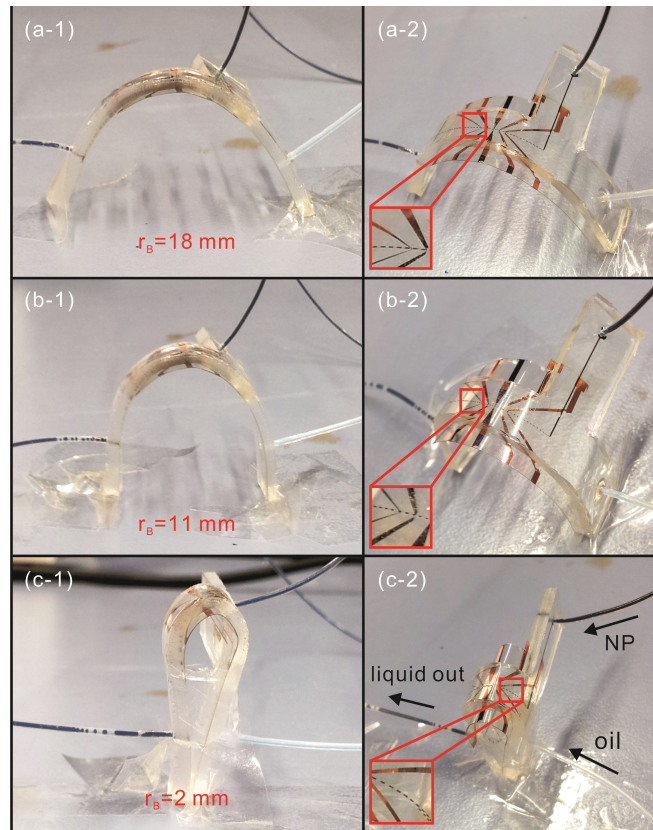


**Fig. S7** | Performance of the flexible magneto-resistive device when it is filled with liquid to produce emulsion droplets during bending tests. The device is gradually bent to different radius of 18 mm (a-1, a-2), 11 mm (b-1, b-2) and 2 mm (c-1, c-2).

**Correlation of the droplet size with the detection peak width:** We produced a train of droplets with different sizes and the detection result is shown in **Fig. S8**. We identified each droplet via monitoring with a digital microscope (INSIZE, ISM-PM 160L, resolution: 10  $\mu\text{m}$ ) which allows us to correlate detection peaks with the monitored emulsion droplets. When emulsion droplets evolve from bigger size (blue area) when they completely fill the channel to smaller size when they are smaller than the channel width (red area), the detection peak patterns evolve concomitantly, indicating that the device is capable of real time monitoring the evolution of droplet shape.

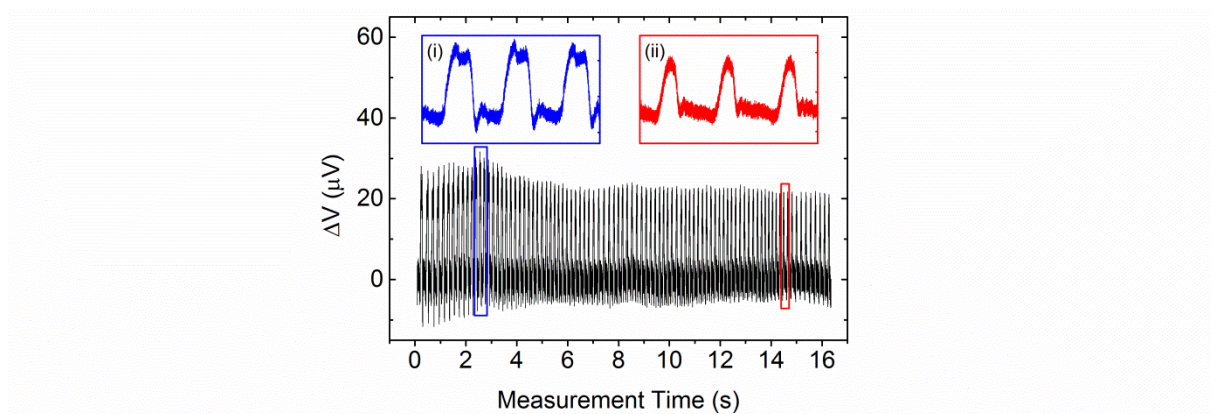


**Fig. S8** | Real time detection of a train of magnetic emulsion droplets with various sizes. Inset-(i) and inset-(ii) Magnification of the areas marked by blue and red rectangles in the main plot, respectively.

**Theoretical calculation of the dependence of effective magnetic stray fields on the droplet size:** As mentioned, the reduction of the signal amplitude shown in **Fig. S8** is ascribed to the reduction of the droplet volume when droplets are smaller than the channel dimension. This leads to both a reduction of the total amount of magnetic contents in a droplet as well as the coverage of the sensor surface by a droplet. To address the dependence of the signal amplitude on a droplet with decreasing volume, a dipole field model is proposed to simulate the case when a droplet has size smaller than the channel dimension. Several assumptions have been made: when a droplet is smaller than the channel dimension, it takes a spherical shape; stray fields from a spherical droplet are simulated as a magnetic dipole, which can be given by:

$$B(\mathbf{m}, \mathbf{r}) = \frac{\mu_0}{4\pi} \left( \frac{3\mathbf{r}(\mathbf{m} \cdot \mathbf{r})}{r^5} - \frac{\mathbf{m}}{r^3} \right)$$

with  $B(\mathbf{m}, \mathbf{r})$  being magnetic flux density at the position described by the vector form  $\mathbf{r}$ ,  $\mu_0$  being the permeability, and  $\mathbf{m}$  being the magnetic dipole moment.

Therefore, the effective stray fields of a droplet acting on a GMR sensor is given by averaging the total stray fields over the sensing volume:

$$B_s(\mathbf{m}, \mathbf{r}) = \iiint \left[ \frac{\mu_0}{4\pi l_s w t} \left( \frac{3\mathbf{r}(\mathbf{m} \cdot \mathbf{r})}{r^5} - \frac{\mathbf{m}}{r^3} \right) \right] dx dy dz$$

Here  $w$  is the width of the sensor,  $l_s$  is the length of the sensor,  $t$  is the thickness of the sensor. As  $t$  is much smaller than the total distance of the droplet from the sensor surface, the vertical variation of the stray fields on a GMR sensor is neglected. We only consider the stray field distribution over a sensor area.

As shown in **Fig. S9a**, the origin of the coordinate system is set at the center of the sensor surface. A droplet is flowing across a GMR sensor stripe ( $w$ : 6  $\mu\text{m}$ ,  $l_s$  100  $\mu\text{m}$ ) along the x axis. We calculate the effective stray fields for a droplet with size of 100, 60, and 20  $\mu\text{m}$ , respectively when it crosses the sensor along the x direction. The distribution of the effective stray fields corresponds to the detection signal measured by the GMR

sensor. We observe that the shape of the simulated stray fields agrees well with the detection signal in **Fig. S8**. Also the effective stray fields decrease with the size of the droplet (**Fig. S9b**), which is indicative of the potential of the device to monitor the change of the transverse dimension of a droplet when it is smaller than the channel. It is advantageous to use the device for monitoring the droplet formation process under different formation mechanisms in real time. The calculation of the stray fields dependence on the droplet size gives hints on the limit of detection of the droplet size when it is encapsulated with i.e., 37.5 mg/ml of magnetic nanoparticles (corresponding to  $\sim 30 \mu\text{V}$  voltage signal), which is about  $10 \mu\text{m}$  in diameter. The limit of detection of the droplet size by the device is comparable to the width of the GMR sensor stripe.

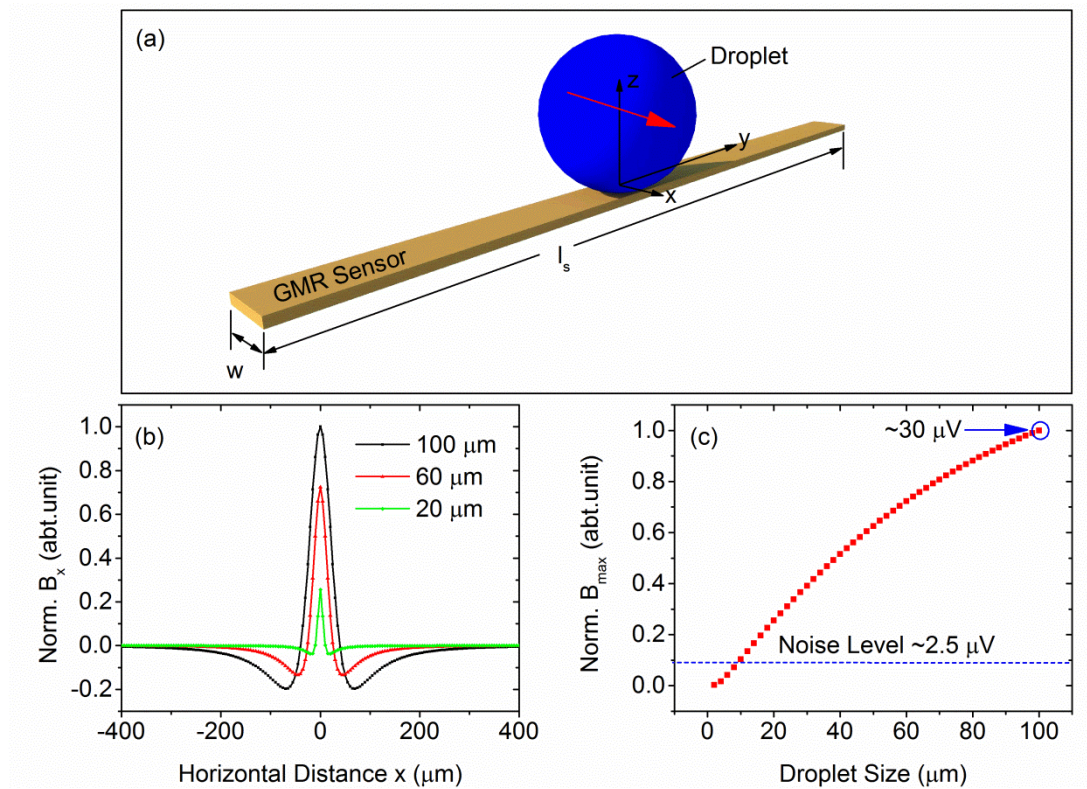


**Fig. S9** | (a) Schematic sketch of a droplet on the surface of a GMR sensor stripe. The width of the sensor is  $w$ , and the length is  $l_s$ . The magnetization of a droplet is indicated by the red arrow, which is along the  $x$  axis (b) Distribution of the effective stray fields on droplets of different sizes. (c) Dependence of the amplitude of the effective stray fields on the droplet size.

**Dependence of the signal on the concentration of magnetic nanoparticles** We measured emulsion droplets of volume around 1 nl encapsulating various concentrations of magnetic nanoparticles. The signal dependence on the concentration of magnetic nanoparticles is shown in **Fig. S10**. With a noise level of  $2.5 \mu\text{V}$ , we can estimate the limit of detection of our current setup is about 4 mg/ml for an emulsion droplet of 1 nl.

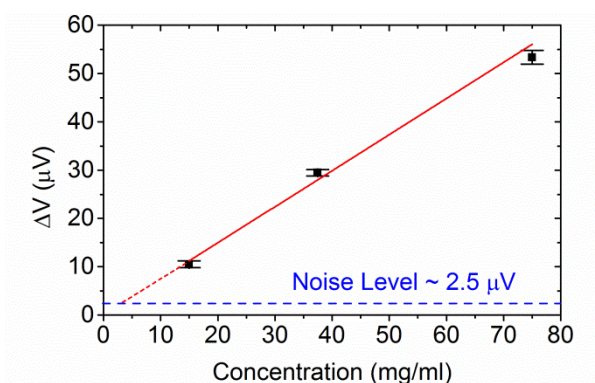


**Fig. S10** | Dependence of signal voltage on the concentration of magnetic nanoparticles encapsulated in a droplet of 1 nl.

**Comparison of the sensitivity of devices** So far, several works have reported on the detection of magnetic emulsion droplets with magnetic sensors. For comparison, we summarize these data in a table:

References	Substrates	Sensor	Sensitivity	Targets	LOD <sup>‡</sup>
[s4]	Rigid Silicon	Spin valve	0.077%/Oe	Droplets loading $\sim 5 \times 10^8$ magnetic nanoparticles with size of 20 pl	NA <sup>‡</sup>
[s5]	Rigid Glass	Planar hall effect sensor	NA <sup>‡</sup>	Droplets loading magnetic nanoparticles (40 pl)	$2 \times 10^{-10}$ emu for droplets of 40 pl; Channel height: 10 $\mu$ m
[s6]	Rigid Silicon	GMR multilayers	0.26%/Oe	Droplets loading magnetic nanoparticles of different sizes ranging from 20 nl $\sim$ 400 nl	2 mg/ml for $\sim$ 100 nl droplets; Channel height: 400 $\mu$ m
<b>Present device</b>	<i>Flexible</i> PET	GMR multilayers	0.4%/Oe	Droplets loading magnetic nanoparticles with different sizes ranges from 0.5 pl $\sim$ 2 nl	1 nl droplets loading 4 mg/ml of particles or 0.5 pl droplets loading 37.5 mg/ml of particles; $2 \times 10^{-10}$ emu; Channel height: 100 $\mu$ m

‡ NA: not available; LOD: limit of detection;

A comparison can be made between our devices with the one in Ref [s5]. In Ref [s5], the LOD of magnetic moment for a droplet of 40 pl is about  $2 \times 10^{-10}$  emu. This is provided when the Hall sensor is integrated in a microfluidic channel with a height of 10  $\mu$ m.

Considering the susceptibility of the ferrofluid particles (Ferrotec, EMG 700 series, [s7]) we used ( $\chi = 12.57$ ), the concentration of particles (5.8 % vol) and the field applied to magnetize the particles (about 15 Oe), the magnetization of a droplet loading such supplied concentration of ferrofluid particles is  $\sim 0.87$  emu/cm<sup>3</sup>.

The minimum detectable volume of droplets is approximately 0.5 pl (10  $\mu$ m in diameter, in Fig. S9), which assumes that the droplets locate on the surface of the sensor. Thus, the LOD of the droplet of 0.5 pl with the device corresponds to a magnetic moment of about  $2 \times 10^{-10}$  emu, which is calculated by the following formula:  $m = V \cdot c \cdot M$ , with  $m$  being magnetic moment,  $c$  being the concentration of ferrofluid

particles (50%),  $V$  being the volume of droplets (0.5  $\mu\text{l}$ ), and  $M$  being the magnetization (0.87 emu/cm<sup>3</sup>). This value is comparable to that reported in Ref [s5].

## References:

- [s1] Y. Chen, Y. Mei, A. Malachias, J. Ingolf Mönch, R. Kaltofen, O. G. Schmidt, *J. Phys. Condens. Matter* **2008**, *20*, 452202.
- [s2] G. Binasch, P. Grünberg, F. Saurenbach, W. Zinn, *Phys. Rev. B* **1989**, *39*, 4828–4830.
- [s3] J. Loureiro, P. Z. Andrade, S. Cardoso, C. L. da Silva, J. M. Cabral, P. P. Freitas, *Lab Chip* **2011**, *11*, 2255–61.
- [s4] N. Pekas, et al., *Appl. Phys. Lett.*, **2004**, *85*, 4783.
- [s5] I. Jeong, et al., *Journal of Magnetism*, **2012**, *17*, 4, 302.
- [s6] G. Lin et al., *Sci. Rep.*, **2013**, *3*, 2548.
- [s7] [https://ferrofluid.ferrotec.com/index.php?id=audioFluid&vfp\\_id=110](https://ferrofluid.ferrotec.com/index.php?id=audioFluid&vfp_id=110)